ACS APPLIED MATERIALS & INTERFACES

Research Article

www.acsami.org

Ultrathin Suspended Nanopores with Surface Plasmon Resonance Fabricated by Combined Colloidal Lithography and Film Transfer

Juliane Junesch[†] and Takumi Sannomiya*[,‡]

[†]Institute of Biomedical Engineering, ETH Zürich, Gloriastrasse 35, 8092, Zürich, Switzerland

[‡]Department of Metallurgy and Ceramics Science, Tokyo Institute of Technology, 2-12-1, Ookayama, Meguro-ku, Tokyo, 152-8552, Japan

Supporting Information

ABSTRACT: Suspended plasmonic nanopores in ultrathin film layers were fabricated through a simple and widely applicable method combining colloidal lithography and thin film transfer, which allows mass production of short-range ordered nanopore arrays on a large scale. By this combined method, mechanically stable and flexible free-standing nanopore membranes with a thickness down to 15−30 nm were produced. The plasmon resonances of the ultrathin plasmonic nanopores fabricated in AlN/Au/AlN trilayer and single layer Au membranes were tuned to lie in the vis−NIR wavelength range by properly designing their dimensions. The optical responses to the refractive index changes were tested and applied to adlayer sensing. The trilayer nanopore membrane showed a unique property to support water only on one side of the membrane, which was confirmed by the resonance shift and comparison with numerical simulation. Pore size reduction down to 10 nm can be achieved through additional material deposition. The filtering function of such pore-size-reduced conical shaped nanofunnels has also been demonstrated. The presented nanopore fabrication method offers new platforms for ultrathin nanopore sensing or filtering devices with controlled pore-size and optical properties. The film transfer technique employed in this work would enable the transformation of any substrate-based nanostructures to free-standing membrane based devices without complicated multiple etching processes.

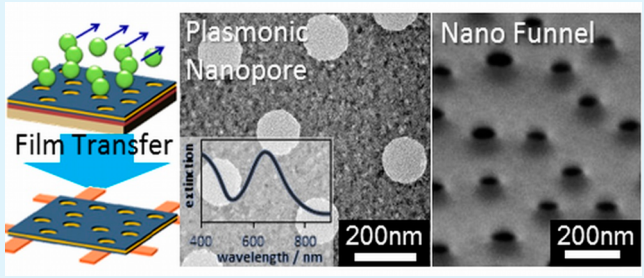

KEYWORDS: *nanopore, colloidal lithography, surface plasmon resonance, transmission electron microscopy*

INTRODUCTION

Transport of ions or molecules through tiny holes, such as protein based nanopores or nanochannels, is a very prominent feature in nature, used for DNA replication, cellular signaling and communication or viral infection. To gain better insight into these physiological processes, nanometer sized holes in a solid state membrane that connect two compartments can be used to mimic these biological nanopores and to study their functions.[1,2] The advantages of these synthetic nanopores over the natural ones are their high stability, size controllability, and adjustable surface properties.[3] They are versatile biosensing tools at the single molecule level[4,5] that can be used for measuring DNA,[6−9] RNA,[10] proteins,[11−13] carbon nanotubes,[14] nanoparticles,[15] or antibody−antigen interactions.[16] In addition, nanopores can be used as filtering or capturing device for molecules,[17] viruses,[18−20] or bacteria.[21] When covered with a lipid bilayer membrane, transport processes through the membrane can also be investigated.[22,23] Typical readout is thereby based either on ionic current measurement, which varies by the passage of target analytes through a single nanopore at a fixed applied potential, or on optical detection of the translocation or binding events of the target molecules. While ionic current readout unavoidably becomes serial unless the multiple electrodes are well separated, optical readout can be easily parallelized by imaging. For the optical sensing, surface plasmon resonance (SPR), which is sensitive to local refractive index (RI) changes caused by medium change or binding events, has been successfully used for sensitive optofluidic sensing devices.[22,24−26]

However, conventional fabrication processes for solid state nanopores are expensive and time-consuming since focused ion beam[27,28] or electron beam systems[29] followed by multiple etching steps are required. Furthermore, large scale production remains a major challenge for these serial patterning methods. Scalability is especially necessary for membrane transport devices with multiple detection elements for parallel readout. Moreover, most current nanopore devices are based on relatively thick (>50 nm) supporting substrates which may cause undesired optical interference,[30−32] high flow-through resistivity, or reduced spatial resolution in ionic current based molecular detection. Drilling a hole through the thick support material also involves additional complex masking and etching processes.

Received: November 28, 2013
Accepted: April 4, 2014
Published: April 4, 2014

To overcome these problems, we developed a simple and widely applicable fabrication technique based on colloidal lithography[33] and a thin film transfer method.[34] This method provides a much simpler, quicker, and inexpensive alternative for producing multiple nanopores on a large scale. Colloidal lithography has been commonly used to produce nanostructures on large areas without costly instrumentation.[31,35,36] The subsequent film transfer can be done onto various supporting materials. We used transmission electron microscopy (TEM) grids, which makes it possible to directly characterize the detailed nanostructures including the crystallinity of the nanoporous membrane. Such nanostructural analysis is often overlooked in plasmonic devices, although it has noticeable influences on their optical properties and stability of the nanostructures of relatively mobile noble metal atoms.[35] With this method, suspended nanopore arrays as thin as 15 nm can be readily produced out of a wide variety of materials, while controlling the pore size and shape, as long as the deposited film are etchant resistant and free from asymmetric intrinsic stress. We fabricated nanopores of different sizes in various materials such as carbon, aluminum nitride (AlN), and gold (Au) as well as multilayers of these materials. The nanoporous films show high stability and robustness, which allows application to sensing or filtering in a broad variety of conditions. Plasmonic nanopore arrays in AlN/Au/AlN trilayer films and single Au films were fabricated, of which optical responses for RI sensing were characterized by medium changes and protein adsorption. We also succeeded in shrinking the initial pore opening size down to 10 nm through additional material deposition although the relative pore size distribution increased. This results in conical shaped pores, or "nanofunnels," which were used as a particle filtering/capturing device.

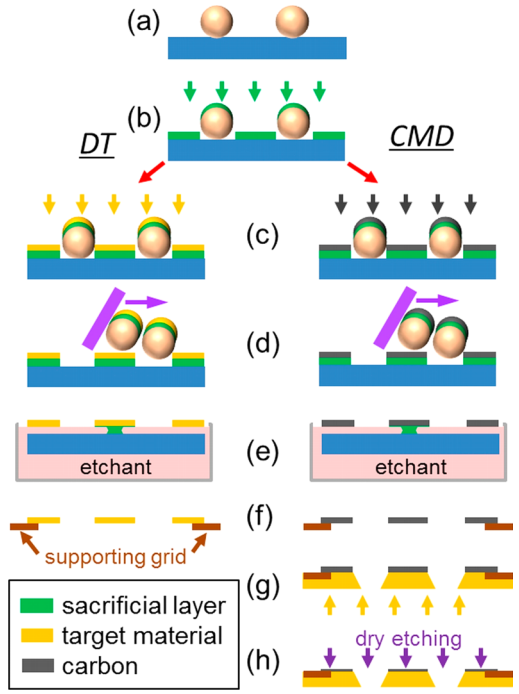

Figure 1. Schematized flowchart of the nanopore fabrication process and pore size control. The left column corresponds to the direct deposition and transfer (DT) method and the right to the carbon mediated deposition (CMD) method. (a) Deposition of polystyrene (PS) colloids on a solid substrate. (b) Sacrificial aluminum (Al) layer deposition. (c) Membrane material (target material or carbon) deposition. (d) Lift-off by squeegee technique. (e) Film delamination by wet-etching the sacrificial layer. (f) Transfer to a supporting grid. (g) Target material deposition for CMD. (h) Removal of the initial carbon by dry etching.

MATERIALS AND METHODS

Nanofabrication Procedure. The fabrication procedure for the suspended nanopores is schematically outlined in Figure 1. It is based on a two-step process, consisting of colloidal lithography[33] and a thin film transfer method.[34] Colloidal lithography allows large area patterning of short-range ordered (SRO) colloid masks.[33] At the first step, polystyrene (PS) colloids are deposited onto a substrate (Figure 1a). On top of this colloidal mask, a thin aluminum (Al) layer is deposited, which serves as sacrificial layer (Figure 1b). For the following steps, two different routes can be chosen: The nanopores can be fabricated either directly by film deposition and transfer (DT, Figure 1 left column) or by carbon mediated deposition (CMD, Figure 1 right column), where the desired films are deposited on a previously produced carbon nanopore membrane that is dry-etched afterward. After the material deposition (Figure 1c), the colloids are removed by rubbing the ethanol-wetted surface with the edge of a scraper that is made out of soft polymer material (Figure 1d). This "squeegee lift-off" technique is less harsh to the film compared to the commonly used tape lift-off and has previously been used for mask on metal lithography[31] or to remove lipid vesicles from a planar surface.[37] In order to exfoliate the nanopore array from the substrate, the samples are placed on the surface of 1 M hydrogen chloride (HCl) solution such that the nanopore film surface remains exposed to air, while the sacrificial Al layer is in contact with HCl and etched from the side (Figure 1e). After the Al layer is fully etched, the nanopore film is separated from the substrate and can then be redeposited on a desired support (Figure 1f). We used TEM copper (Cu) grids (#300, Nisshin, Japan) as the supports and transferred the films onto the grids by immersing them into the solution with tweezers and skimming the floating films.

The CMD method (Figure 1, right column), where the desired films are deposited on top of an already suspended carbon nanopore film, extends the fabrication possibilities from the DT method; a higher variety of materials, which are not suited for wet-etching, can be deposited on top of the amorphous carbon. Furthermore, the hole size can be reduced and the shape changed through additional deposition of carbon or dielectric materials such as AlN (Figure 1g). By adjusting the sample source distance, angle, and deposited film thickness, the shrinking rate can be tuned accordingly. The initial carbon film can then be removed by dry etching using oxygen plasma or UV ozone (Figure 1h).

Colloidal Lithography. Silicon substrates were cleaned by rinsing with ethanol and deionized (DI) water and blow-dried under a nitrogen (N_2) flow. After hydrophilization by oxygen plasma (~1 Pa, 18W, Harrick Plasma PDC32G, USA) for 5 min, a solution of aluminum chloride hydroxide (c = 5%, Summit Research Laboratories, USA) was deposited on the substrate, followed by rinsing with DI water and N_2 blow drying. This treatment creates a positively charged surface to enhance the adsorption of the negatively charged PS colloids. A 0.05 wt % suspension of 100 nm (Invitrogen, US, standard deviation: 8%) or 147 nm (Microparticles, Germany, standard deviation: 5%) diameter PS colloids was drop-coated and left 2

min for adsorption, followed by DI water rinse. While the surface is still wet, the PS colloids were fixed by pouring on hot ethylene glycol (130 °C, 5 s), followed by a DI water rinse, and final N_2 blow drying.

Layer Deposition. DC magnetron sputtering was used to deposit aluminum (Al), aluminum nitride (AlN), and gold (Au) (working pressure p = 0.5 Pa, base pressure $<10^{-4}$ Pa). Metallic Al and Au were deposited under an argon (Ar) atmosphere at a flow rate of 6 sccm (standard cubic centimeters per minute). AlN was reactively sputter-deposited under an Ar and N_2 flow (Ar = 4 sccm and N_2 = 3 sccm) using an aluminum target. The thickness was determined from the deposition rates (1.13 nm/min for AlN and 8.00 nm/min for Au), which were calibrated by atomic force microscopy (AFM) measurements in advance. Carbon was deposited by arc-evaporation using a carbon rod. The thickness was monitored by a quartz crystal microbalance as well as transmission spectra of nonstructured films deposited simultaneously.

Multilayer Design for Plasmonic Nanopores. In order to control the plasmon resonance for long-range ordered (LRO) or short-range ordered (SRO) plasmonic pores, the dimension of the pore membranes should be properly designed since the resonance occurs as an interference of the surface plasmon polaritons (SPPs) between the pores.[38,39] The interpore distance, film material, film thickness, as well as the number and order of the layers should be optimized. The resonance condition states that the SPP wavelength matches the characteristic interpore distance Λ, which can be obtained from the radial distribution function (RDF) for SRO arrays. The SPP wavelength in a multilayer system can be calculated from the dispersion relation (DR, see Supporting Information).[39,40] It is also important to retain reasonably long SPP propagation lengths so that one pore can interact with the neighboring pores over a sufficiently strong field. The film thicknesses are designed such that the SPP resonance mode (extinction maximum) lies in the vis−NIR range (details in Supporting Information). For a multilayer structure, we denote the layer material separated by a slash and the thickness in the parentheses without a nanometer unit, e.g., AlN(10)/Au(12)/AlN(6) for a trilayer consisting of 10 nm AlN, 12 nm Au, and 6 nm AlN films. We used 100 nm PS colloid masks for AlN(10)/Au(12)/AlN(6) trilayer films and 147 nm colloid masks for AlN(8)/Au(16)/AlN(8) and single Au films.

Characterization. Transmission electron microscopy (TEM) images were obtained using JEM3010 (JEOL, Japan) at a 300 kV acceleration voltage. High angle tilting images were taken with a JEM2010 (JEOL, Japan) at 200 kV. To obtain high enough contrast for very thin samples, especially for carbon, images were obtained under defocused conditions. By digitally enhancing the weak image contrast, the CCD scintillator pattern in the uniform region may become visible. The dark spot in the middle of some pictures corresponds to dead pixels. Scanning electron microscopy (SEM) imaging was performed with JSM-700F (JEOL, Japan) using the secondary electron detector. SEM Images of the captured colloids inside the nanopore were taken by ULTRA plus (Carl Zeiss, Germany) using the combined inlens and a secondary electron detector.

The extinction spectra were taken under a microscope (Olympus BXFM, Japan) by illuminating the samples with a halogen lamp light source and collecting the transmitted light with a spectrometer (Hamamatsu C10083MD, Japan) in a circular spot of 11 μm in diameter. Extinction was defined as $\Omega = \ln(I_0/I)$, where I_0 is reference intensity and I is transmission intensity. Fourier low-pass filtering was applied with cutoff in the range of 0.03−0.05 nm^{-1} to remove the high frequency noise. The reference spectrum was recorded in air, which introduced a small offset for the spectra taken in the flowcell. This offset was corrected by normalizing the extinction spectra to the same baseline. A custom-made flow cell was used for the measurement under aqueous conditions (see Supporting Information). Linear baseline correction was applied for the kinetic measurement. Ultrapure water (milli-Q, Millipore Corporation, Japan; resistance: ∼18 MΩcm; TOC: < 4 ppb) was used for sensing experiments. The neutravidin (NeutrAvidin 60kD, Pierce) adsorption was measured in a HEPES buffer solution (10 mM 4-(2-hydroxyethyl)-1-piperazineethanesulfonic acid with 150 mM NaCl and pH adjusted to 7.4).

Simulation. To analyze the optical property of the fabricated plasmonic nanopores, numerical simulation was conducted using a multiple multipole program (MMP) in OpenMaX software package.[41] SRO structures are in general difficult to simulate because a huge calculation space must be defined, which is extremely memory- and time-consuming for plasmonic structures. It was previously found that the SPP resonance position and shift of the SRO plasmonic nanoholes fabricated by colloidal lithography well corresponds to those of the LRO plasmonic nanoholes with hexagonal arrangement when the interference length of LRO equals the characteristic spacing of SRO obtained from the RDF.[40] Hexagonal arrays were therefore used to imitate the SRO nanopores. Rhombic periodic boundaries of the length 230 and 325 nm were defined for the pore sizes of 100 and 147 nm, respectively, considering the characteristic interference length Λ between 2D hexagonal (1 1) planes. The film thicknesses were set accordingly to those of the experimental systems. The dielectric constants used in the simulation are 1.0, 1.777, and 2.1 for air, water, and AlN, respectively, which are not dispersive. For gold, literature values were used.[42] The transmission intensity was calculated from the efficiency of the Rayleigh expansion located below the calculation cell. The edges of the structures were rounded to avoid singularity.

RESULTS AND DICUSSION

Feasibility of Ultrathin Nanopore Fabrication. As seen in the low-magnification SEM image (Figure 2a) the transferred nanopore film spans evenly and smoothly over the grid. The pores (tiny black dots) are homogeneously distributed in the membrane. Since such thin membranes with a thickness of tens of nanometers are fairly bendable and flexible, it would also be possible to transfer them to uneven or curved surfaces. Very thin membranes and their flexibility can be confirmed by imaging the edge of the membrane (see Supporting Information). Nanopore membranes spanned on different supports are shown in the Supporting Information. Even nanoporous films of 15 nm thickness, as shown in Figure 2b, have high mechanical stability and robustness. It is noted that the asymmetric intrinsic stress causes film curling, and therefore symmetric layering is preferred. Once the films were transferred to the TEM grid and dried, the pore membranes stayed intact after immersion in liquid or rinsing under a low pressure water stream. Special care should be taken so that the water stream flows along the membrane surface to avoid tearing the membrane. The nanopores are stable enough for multiple-time use, which is confirmed by the optical spectrum (Figure S8 in the Supporting Information) and can also be confirmed in the SEM image after use as shown in the filtering measurement.

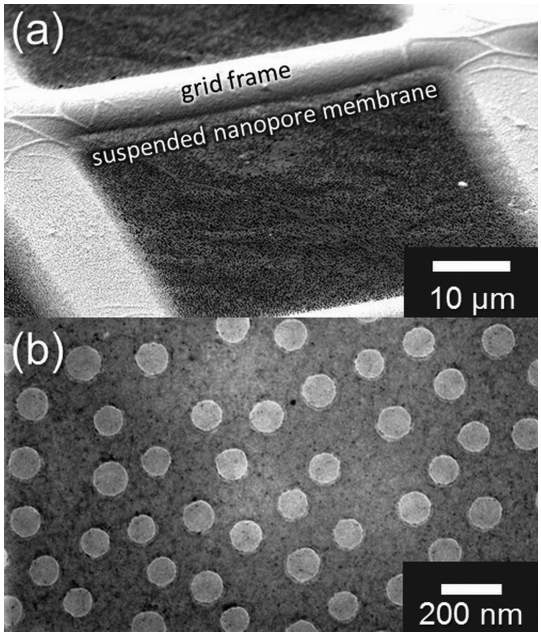

Figure 2. (a) SEM image taken under an angle of 40° of the AlN/Au/AlN nanopore film after transfer on a TEM Cu grid. The film is spanned straight and evenly over the grid. The square opening is 45 μm, while the frame bar is 38 μm (partially shadowed by the film). (b) Defocused TEM image of 100 nm sized carbon nanopores with 15 nm thickness. The holes are uniform within 6.7% size distribution and round in shape and are arranged in a short-range order (SRO).

However, more systematic durability tests with more statistics would be required to fully quantify the usable number of the cycles. Nanopore samples can also readily be mass-produced: we prepared nine suspended nanopore samples (3 mm diameter TEM grid) out of the original 1 × 1 cm substrate by separating the film. Since these very thin nanopore membranes have lower fluidic resistance compared to thicker pore membranes with supporting materials, less pressure is required to flow the solution through the pores. Furthermore, without a thick support underneath, the RI sensitivity of the plasmonic nanopore is enhanced since the electric field tends to get drawn into the higher refractive index support material than medium.[43−45] The undesired optical interference by the thick dielectric layer can also be avoided.[30−32]

The very thin feature of the fabricated nanopore membrane enables TEM analysis without special sample preparation. The TEM image of the carbon nanopores in Figure 2b shows that the fabricated pores are round and uniform in shape and size. The pores are well arranged in a SRO pattern, which is known to have equivalent optical properties to LRO structures for surface plasmon resonances.[39] By calculating the RDF, the characteristic spacing to the nearest neighbor Λ, corresponding to the effective periodicity in LRO systems, is determined.[31] For the 100 nm SRO pores, we obtained Λ = 190−200 nm and for 147 nm pores Λ = 280−290 nm (see Supporting Information).

Plasmonic AlN/Au/AlN Trilayer Nanopores. AlN/Au/AlN trilayer nanopores with plasmon resonances, as schematically illustrated in Figure 3a, were fabricated both by DT and CMD routes. AlN sandwiching was employed to enhance the crystallinity and interface smoothness of Au.[40,46] The TEM image and diffraction pattern of AlN(10)/Au(12)/AlN(6) nanopores prepared from 100 nm PS colloids by the DT method show that the film is polycrystalline without in-plane preferential crystalline orientation (Figure 3b). The interface between the face-centered cubic (FCC) metal and the wurzite AlN layer in the sputter-deposited multilayer is known to be flat and sharp due to local epitaxy.[46] The in-plane grain size is estimated to be around 20−30 nm from the TEM image, which is larger than the film thickness. High resolution TEM lattice images reveal the Moiré pattern from AlN (100) and Au (220) lattices indicating the coherent crystalline growth with AlN (001) and Au (111) perpendicular to the film plane (Supporting Information). Such good crystallinity and a smooth interface are essential for SPP in ultrathin films, not only because the crystal defects, i.e., grain boundary or stacking fault, damp the SPP resulting in broad and smeared resonance features but also because the surface and interface roughness modulates the thickness within the film.

The optical resonance of the AlN(10)/Au(12)/AlN(6) nanopore was successfully tuned to lie in the vis−NIR range as shown in Figure 3c. In order to test the sensor performance upon RI change, we conducted optical transmission experiments in air and water. Since the suspended nanopore membrane can separate two media, we injected water first only on one side of the nanopore membrane while the other side was kept in air. During this process, we followed the extinction maximum and detected a red-shift of about 50 nm. After injecting water into both sides the spectrum shifted further by 30 nm and remained very stable over time. In Figure 3d, the peak shift over time with respect to the initial position in air is shown as a thick black line. The water injections on one side and both sides were done after 11 and 15 min, respectively, and caused abrupt increases of the peak position. This set of experiments seemingly shows that the pore membrane can support water on one side without wetting the other side, probably owing to the relatively hydrophobic surface property of AlN.[47] In order to gain a better understanding of the immersion processes, we simulated the extinction spectra for the corresponding LRO structures in different immersion configurations: (i) entirely in air, (ii) only top side in water with the pore unfilled, (iii) top side and inside of the pore in water, and (iv) entirely in water. The simulated spectra are shown in Figure 3e, and the resonance shift with respect to the simulated position in air is plotted as rhombuses in Figure 3d, superimposed on the experimental curve. The spectra and in particular the relative resonance shift from air to full immersion in water well match the experimental results, confirming that the pore membrane is completely immersed in water without air bubbles. The slight difference between the experimental and simulated results most probably originates from the difference in the dielectric constants of gold[42] or from experimental errors in the interpore distance or film thickness. The intermediate state where the water is supported on one side in the experiment giving the resonance shift of about 50 nm, which is more than the half of the resonance shift upon full immersion, corresponds well to the simulated configuration of the pore filled with water (Figure 3d). The extinction intensity increase in the spectrum in the experiment (Figure 3c) is also reproduced by the pore filled configuration. These results confirm that the pore is filled with water already in the one-side immersed state and is not blocked by air inside the pore. The hydrophilic nature of metallic gold probably introduces water inside the pores, which then spontaneously evaporates at the pore. The slightly noisy response during the one-side water state in the experiment (Figure 3d) could be due to the

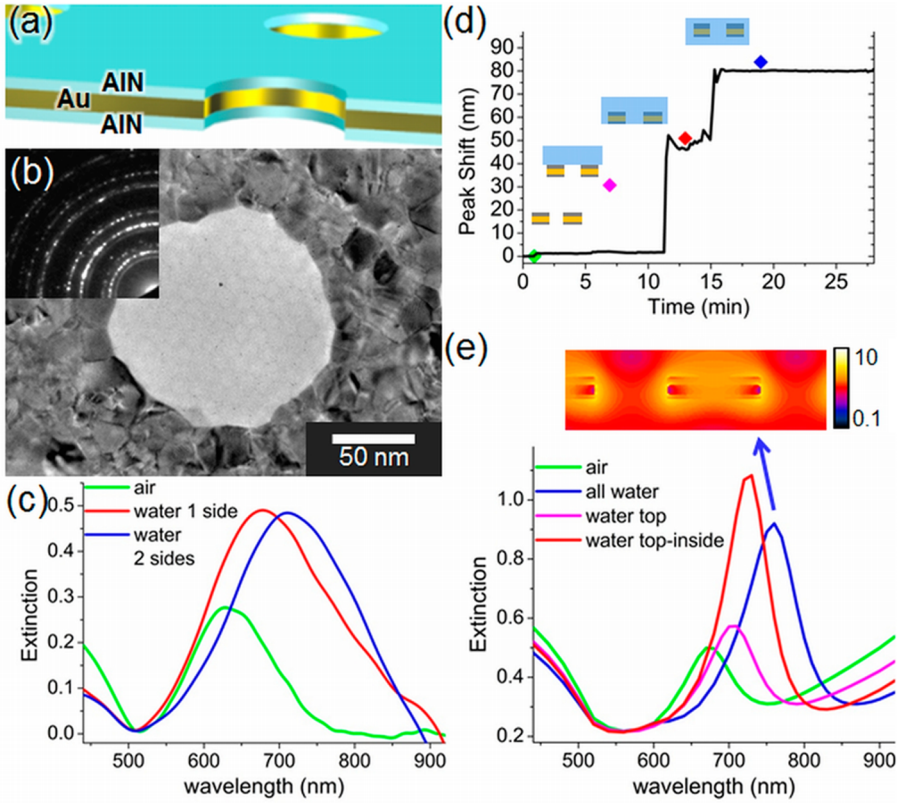

Figure 3. Nanopores in the AlN(10)/Au(12)/AlN(6) trilayer by DT and comparison with the simulation. (a) Schematic illustration of the trilayer pores. (b) TEM image of the trilayer nanopores. Inset: corresponding diffraction pattern. (c) The experimental spectra in air (green), with water on one side (red) and water on both sides (blue). All spectra are normalized to the gold absorption at 510 nm. (d) Experimental resonance peak shift plot (solid black line) first in air (0−11 min), then water on one side (11−15 min), and finally water on both sides (15−28 min). Simulated peak shifts (rhombus, no time dependence) in different water immersion configurations, as illustrated in the graph, are superimposed. (e) Simulated spectra in air (green), the top side immersed (pink), top and inside the hole immersed (red), and fully immersed (blue) in water. The spectra are normalized by the gold absorption at 560 nm. The time-averaged electric field pattern (field enhancement) at the extinction maximum wavelength immersed totally in water is also shown.

dynamics of water evaporation and refilling into the pore. Such a one-side water supporting and nanodrain effect of open-end nanopores that can promote the flow via capillary force and evaporation has been observed previously for SiN/Au nanopores.[48] The time-averaged electric field plot for the extinction maximum wavelength in water (Figure 3e) shows that the field enhancement is distributed evenly around the pore as well as on the membrane, which is typical for the SPP interference mode (extinction maximum). Since the behavior of the liquid in the pore with one side exposed to another medium can be mmonitored, it could be used for e.g. monitoring the air−liquid interface phenomena, such as the Maragoni effect, interdiffusion of different media on each side, and enhancement of molecular concentration in biosensing.[48] From the spectral response by RI change, we could derive medium sensitivities of 142 nm/RIU for water on one side and 236 nm/RIU for water on both sides.

To demonstrate the applicability of the plasmonic nanopore to biosensing, we performed adlayer sensing by monitoring the adsorption of the protein neutravidin. Biomolecular sensing was conducted using 147 nm pores in an AlN(8)/Au(16)/AlN(8) membrane (extinction spectrum in the Supporting Information). After stabilizing the pore membrane in a HEPES buffer neutravidin solution of 20 μg/mL was injected into both sides of the membrane and left for adsorption. The peak shift plot in Figure 4a shows typical adsorption dynamics of a protein layer

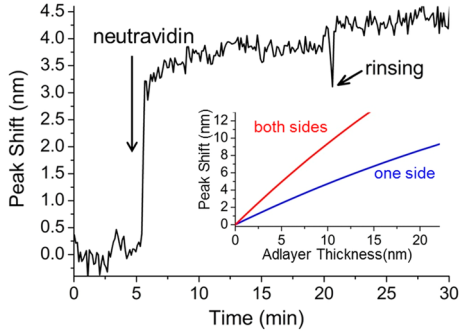

Figure 4. Adsorption curve of neutravidin (20 μg/mL) using 147 nm AlN(8)/Au(16)/AlN(8) nanopores. The inset shows the estimated peak shift as a function of thickness calculated from DR for protein adlayers on one side (blue line) and both sides (red line) of the membrane. Nondispersive RI of 1.45 of the adlayer was used for DR calculation.[49,50]

giving approximately a 4 nm resonance shift. After reaching saturation, the sample was rinsed with HEPES buffer. The peak position then stayed constant over time. The slight discrete jump at the rinsing is probably caused by a small displacement of the nanopore sample by injection. The expected resonance shift of a protein adlayer in this system can be estimated from the DR of the corresponding structure as plotted in Figure 4b. The adsorbed protein monolayer of this size is typically around

4−5 nm,[49] which is in good agreement with the both side coated calculation results.

For the plasmonic nanopores fabricated through the CMD route, it is possible to monitor the removal process of the initial carbon layer. We fabricated an AlN(8)/Au(16)/AlN(8) trilayer on 35 nm thick carbon nanopores made from 147 nm PS colloids. The representative extinction spectra after different oxygen plasma etching time are shown in Figure 5a. The initial

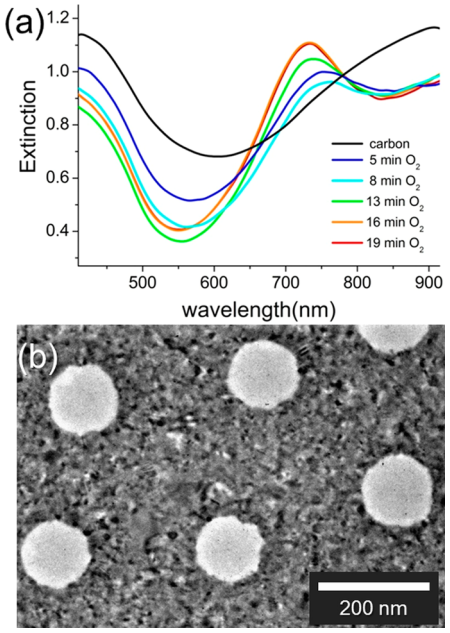

Figure 5. (a) Spectral change of the AlN(8)/Au(16)/AlN(8) membrane fabricated with 147 nm colloid masks during the carbon removal procedure in the CMD method. The initial 35 nm carbon layer was gradually removed by oxygen plasma etching. 16 and 19 min spectra overlap showing the complete removal of carbon. (b) TEM image of the CMD fabricated nanopores after full removal of the initial carbon layer.

spectrum with the full carbon layer (ca. 35 nm) is quite broad, and the extinction maximum lies around 900 nm. However, as the carbon film becomes thinner with longer etching time, the spectral features grow sharper and the extinction maximum shifts to shorter wavelengths because the lossy and high refractive index material is removed. The carbon removal rate at the first few minutes is higher since the peak quickly drops from roughly 900 nm to around 770 nm and gradually blue-shifts after 5 min. After 16 min, the spectrum becomes stable, suggesting that the carbon film is fully etched (Figure 5a). As the carbon is removed, the spectrum of the CMD-fabricated nanopore approaches that of the nanopore with the same dimension fabricated by DT (compare Figure S10, Supporting Information). Details of the analysis of the carbon layer thickness can be found in the Supporting Information. As shown in the TEM image of Figure 5b, the hole shape remains uniform and round, while the additional film deposition causes the pores to shrink approximately to 120 nm in diameter from the initial 147 nm of the PS colloid mask. The smaller hole diameter results in the blue shifting of the extinction minimum.[39]

Plasmonic Au Single Layer Nanopores. Plasmonic nanopores in single layer Au films, as illustrated in Figure 6a, were fabricated by the DT method, which to our knowledge has

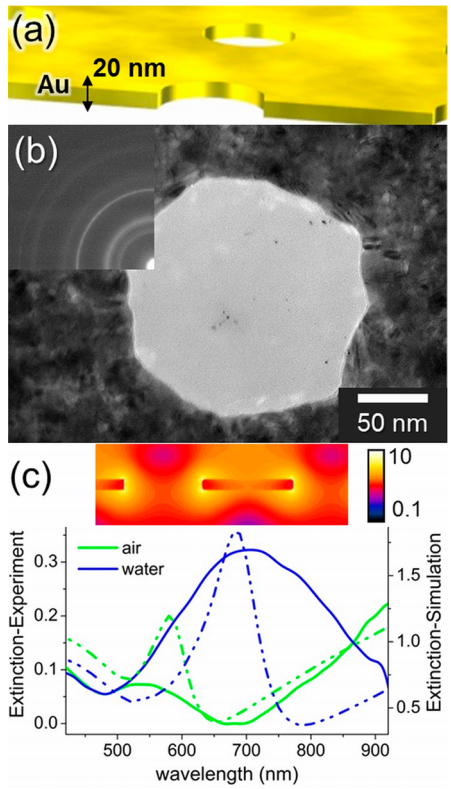

Figure 6. (a) Schematic illustration of the Au single layer nanopores. (b) TEM image of 147 nm size nanopore in 20 nm Au film and its diffraction pattern in the inset. (c) Measured (SRO, straight lines, left axis) and simulated (LRO, dash lines, right axis) extinction spectra in air (green) and water (blue). The simulated time-averaged electric field pattern (normalized field enhancement) at the extinction maximum wavelength in water is shown above the spectrum.

never been produced or studied so far. 147 nm PS colloid masks were employed to produce the pores in a 20 nm Au membrane. We verified that the fabricated film is composed solely of Au by energy dispersive X-ray spectroscopy (EDS), where we detected only the Au peaks and those originating from the supporting Cu grid (Supporting Information).

The TEM image and diffraction pattern prove that only FCC Au is present and is polycrystalline without preferential orientation (Figure 6b). The crystal grain size is smaller (around 5 nm) than those of the AlN/Au/AlN trilayer structures. Significantly more crystalline defects, such as stacking faults and dislocations, than the AlN sandwich trilayer are also visible as line contrasts inside the grains. Due to this low crystallinity, a very broad optical resonance was observed (Figure 6c, straight lines). It is noted that the material property of Au is different from that in the trilayer because the low crystallinity and interface roughening typically gives higher damping and larger effective electron mass, which results in a broader resonance in the spectrum.[35] We further noticed that the Au membrane is unstable under electron beam irritation and that even under ambient conditions the plasmon resonance is slightly changing due to transformation in morphology (see Supporting Information).

RI sensing was performed by following the extinction maximum while changing the surrounding RI. The resonance shifts from 536 nm in air to 707 nm in water, resulting in a sensitivity of 518 nm/RIU (Figure 6c, straight lines). This value is among the highest for plasmonic sensing in vis−NIR,

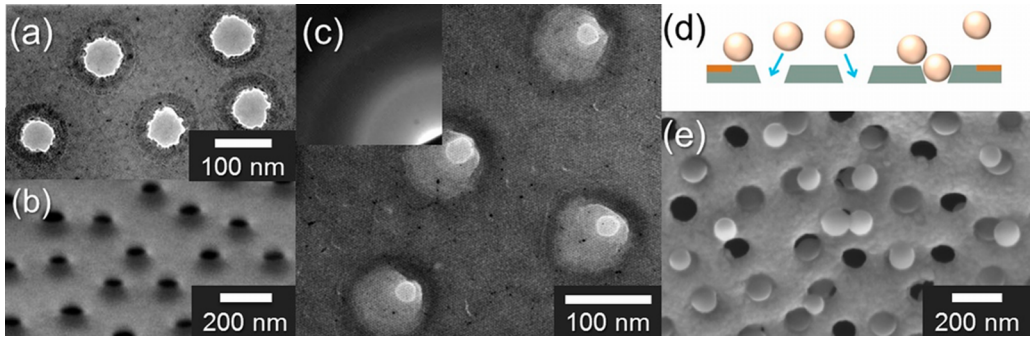

Figure 7. Size reduction of originally 100 nm nanopores by additional material deposition. (a) TEM image of nanopores that were size-reduced to ~60 nm in diameter by depositing 85 nm AlN. (b) Corresponding SEM image observed from the smaller opening side at a tilted angle. (c) TEM image of carbon nanopores with ~10 nm opening by additional angled deposition. Inset: diffraction pattern showing only carbon amorphous structure. (d) Schematic illustration of colloid capturing where colloids were introduced from the larger pore opening side and let flow through the pore to the narrower side. (e) SEM picture after the colloid capturing in the carbon nanofunnels, taken from the smaller opening side. Dark pores are empty, and gray ones are filled by colloid particles.

although the figure of merit (~2.5) is low due to the peak broadening.[51] The peak shift sensitivity is higher than the AlN/Au/AlN trilayer system, which can be explained from the DR of the Au single layer (see Supporting Information) and from the fact that the sensitivity is highest in the vicinity of the Au surface which is blocked by AlN in the sandwich film. The resonance peak position and the shift by the medium change of the SRO nanopores are reproduced by the simulation of the LRO hexagonal pore array with the corresponding interference length (Figure 6c, dashed lines). The much broader feature of the resonance in the experiment than in the simulation is mainly because of lower crystallinity of the single layer Au as well as of distributed interpore distance in SRO. We also tried one-side medium immersion as done in the AlN/Au/AlN trilayer, which however was not possible because of the hydrophilic surface property of pure gold films. This conversely means that the hydrophilic single-layer gold membrane spontaneously wets the whole surface.

Pore Size Control. Through additional material deposition on the nanopore membrane, it is possible to uniformly shrink the pore opening as shown in the CMD process in previous sections. By depositing a thick additional layer, the nanopore grows in a conical shape, which results in "nanofunnels" (Figure 7a). With this shrinking method, we can tune the hole size without changing the characteristic interpore distance of the initial SRO, which is not possible by colloidal lithography itself. Colloids with a size below 100 nm typically have poor size homogeneity, and attempts to shrink the PS particles after colloidal self-assembly by UV ozone caused lift-off problems as the colloids could not be removed from the surface. Through changing the deposition parameters, such as the thickness of the evaporated material, the distance and angle between the source and substrate, the shape and geometry of the nanopores could be controlled similar to the shrinking method by atomic layer deposition.[52] For pore shrinking, amorphous material such as carbon (e.g., Figure 7c) is preferable to crystalline material (e.g., Figure 7a) in order to avoid roughened edges due to faceting and orientation dependent crystalline growth. This pore-size reduced carbon nanopore membrane can be used as the base film in the CMD approach to fabricate small nanopores out of other materials with arbitrary thicknesses.

By additional sputter-deposition of 85 nm AlN, the pore size was reduced by ~40% (Figure 7b), and by angled carbon deposition, we could even close the opening to ~10 nm (Figure 7c), which is comparable to the size of biomolecules. As the growth rate is larger on one side, asymmetric conical holes are produced by angled deposition. These nanofunnel structures are also advantageous for nanoelectrochemistry, as conical nanopores can be used for rectifying the ion current.[53,54] Furthermore, the conical shape is beneficial to selectively capture and detect particles,[15] viruses,[18] or bacteria[21] larger than the defined pore size.

To test the capturing abilities of the nanofunnels, we used size-reduced ~85 nm carbon pores, which were originally 100 nm, and captured 100 nm PS colloid particles. The nanopore sample was first fully immersed into water, and the colloid solution was then introduced from the larger pore opening side (Figure 7d) to the other side, thus letting them flow through the pores and getting captured. Thereby we applied a pressure difference of ca. 7 kPa between the two sides (configuration in Supporting Information). The SEM picture in Figure 7e, taken from the smaller opening side after colloid capturing, shows that colloids are trapped into the nanofunnels, while just some smaller colloids or those that entered through larger openings are found adsorbed next to the pores on the downstream side of the membrane. Some colloid particles may have been displaced during the drying process before SEM sample preparation. This SEM image also confirms that the filtering in liquid, drying, and vacuum pumping processes does not destroy the membrane. The capturing dynamics monitored by plasmonic nanopores is presented in the Supporting Information. On the other hand, the filtering experiment also reveals that the pore and colloid particle sizes are not perfectly uniform since not all the particles are captured. Because the distribution of the original pore size depends on the colloid mask, more uniform colloid suspension produced through better controlled ripening processes should be applied to improve the uniformity of the pores.[55,56] The pore size uniformity could be further improved by glancing angle deposition with an appropriate deposition angle so that the material is deposited on the side walls of the larger pores, but the side walls of smaller pores are self-shadowed.[57]

CONCLUSION

We have demonstrated a novel technique to produce suspended nanopores in ultrathin films. Our method combines colloidal lithography and thin film transfer and allows large scale production with a high yield. Since no expensive and time-

consuming setups or special requirements for the substrate are needed, this combined method would be a low-cost and simple alternative to the conventional solid state nanopore fabrication techniques. The ultrathin nanopore membranes are mechanically stable, flexible, and could be transferred to a wide variety of substrates or supports, although a more systematic test would be required to quantify the long-term durability. We successfully prepared nanopores in AlN/Au/AlN trilayers as well as Au single layers with plasmonic resonances in the vis−NIR wavelength range. Those plasmonic nanopore membranes can be prepared either directly (DT) or starting from carbon nanopores (CMD). These two possible fabrication routes offer application of nearly any material depending on the suitability of the film material to the wet-etching or to the dry carbon etching by oxygen plasma. We also tested the RI sensitivity of the plasmonic nanopores by optical transmission measurements in air and water. For the AlN(10)/Au(12)/AlN(6) trilayer film with a total thickness of 28 nm, we determined the bulk medium sensitivity to be 236 nm/RIU, and in the case of pure 20 nm thick Au ones, 518 nm/RIU. Ultrathin single Au films however have worse crystallinity and stability compared to the AlN sandwich trilayers with smooth interfaces. The very thin nature of such plasmonic nanopores is advantageous for transport measurement because of the low flow resistance.[58] It was also possible to support and measure water only on one side of the trilayer pore membrane with the other side exposed to air. The capillary force, when one side is exposed to air, can introduce spontaneous flow toward the pore location, which could overcome the diffusion limited sensitivity for low analyte sensing.[48] This unique medium separating property of gold-based nanopore membranes might also be applicable to catalytic electrodes, such as in lithium−air fuel cells.[59−62] The ultrathin suspended membrane structure is beneficial for optical sensing devices because there is no hindering influence of the underlying substrate or support, which is the case for most currently used devices.[63] Other applications, such as electrochemical measurements[16,64,65] or ion current devices,[66,67] would also benefit the ultrathin nanopore membranes in terms of temporal and spatial resolution. Through additional material deposition, the pore size can be further reduced, resulting in conical shaped "nanofunnels." It was possible to shrink the carbon nanopore size down to ∼10 nm while keeping the pore shape round, although the relative size distribution increases due to the original size distribution of the colloid masks. Such nanofunnels with the opening size comparable to molecular scales would be useful for single molecule sensors, molecular sieves, or capturing devices. We demonstrated the particle capturing capability using PS colloids. Tunable pore size and material selectivity would be useful for lipid membrane formation by vesicle rupture because the tiny pore size as well as hydrophobic and flat surfaces is favored.[68,69] Such nanopores and nanofunnels could serve as new platforms to study membrane transport or for filtering and sensing devices.[70] Finally, we also note that the presented film transfer technique can be applied to other nanopatterning methods to produce free-standing membrane consisting of various nanostructures without costly multiple masking and etching steps.

■ ASSOCIATED CONTENT

Ⓢ Supporting Information

Calculation of the radial distribution function, dispersion relation of the multilayers, energy dispersive spectroscopy (EDS) data, detailed TEM analysis, low magnification SEM images on different supports, stability test, optical spectra of nanopores in different AlN/Au/AlN trilayer, carbon layer sensing, optical detection of colloid capturing, the flow cell configuration, and size distribution of the pores. This material is available free of charge via the Internet at http://pubs.acs.org.

■ AUTHOR INFORMATION

Corresponding Author

*E-mail: sannomiya@mtl.titech.ac.jp.

Author Contributions

The manuscript was written through contributions of all authors. All authors have given approval to the final version of the manuscript.

Notes

The authors declare no competing financial interest.

■ ACKNOWLEDGMENTS

We thank Dr. A. Dahlin, Prof. J. Vörös, and Prof. J. Shi for scientific discussions and valuable inputs. This work was funded by the Japanese Society for the Promotion of Science (JSPS), Tokyo Institute of Technology, ETH Zurich, Mizuho Foundation for the Promotion of Science and Iketani Science and Technology Foundation.

■ REFERENCES

(1) Martin, C. R.; Siwy, Z. S. Learning Nature's Way: Biosensing with Synthetic Nanopores. *Science* **2007**, *317*, 331−332.

(2) Griffiths, J. The Realm of the Nanopore. *Anal. Chem.* **2008**, *80*, 23−27.

(3) Dekker, C. Solid-state Nanopores. *Nat. Nanotechnol.* **2007**, *2*, 209−215.

(4) Miles, B. N.; Ivanov, A. P.; Wilson, K. A.; Dogan, F.; Japrung, D.; Edel, J. B. Single Molecule Sensing with Solid-State Nanopores: Novel Materials, Methods, and Applications. *Chem. Soc. Rev.* **2013**, *42*, 15−28.

(5) Howorka, S.; Siwy, Z. Nanopore Analytics: Sensing of Single Molecules. *Chem. Soc. Rev.* **2009**, *38*, 2360−2384.

(6) Fologea, D.; Gershow, M.; Ledden, B.; McNabb, D. S.; Golovchenko, J. A.; Li, J. Detecting Single Stranded DNA with a Solid State Nanopore. *Nano Lett.* **2005**, *5*, 1905−1909.

(7) Li, J.; Gershow, M.; Stein, D.; Brandin, E.; Golovchenko, J. A. DNA Molecules and Configurations in a Solid-State Nanopore Microscope. *Nat. Mater.* **2003**, *2*, 611−615.

(8) Kowalczyk, S. W.; Tuijtel, M. W.; Donkers, S. P.; Dekker, C. Unraveling Single-Stranded DNA in a Solid-State Nanopore. *Nano Lett.* **2010**, *10*, 1414−1420.

(9) Storm, A. J.; Storm, C.; Chen, J.; Zandbergen, H.; Joanny, J.-F.; Dekker, C. Fast DNA Translocation through a Solid-State Nanopore. *Nano Lett.* **2005**, *5*, 1193−1197.

(10) Skinner, G. M.; van den Hout, M.; Broekmans, O.; Dekker, C.; Dekker, N. H. Distinguishing Single- and Double-Stranded Nucleic Acid Molecules Using Solid-State Nanopores. *Nano Lett.* **2009**, *9*, 2953−2960.

(11) Plesa, C.; Kowalczyk, S. W.; Zinsmeester, R.; Grosberg, A. Y.; Rabin, Y.; Dekker, C. Fast Translocation of Proteins through Solid State Nanopores. *Nano Lett.* **2013**, *13*, 658−663.

(12) Han, A.; Creus, M.; Schürmann, G.; Linder, V.; Ward, T. R.; de Rooij, N. F.; Staufer, U. Label-Free Detection of Single Protein Molecules and Protein−Protein Interactions Using Synthetic Nanopores. *Anal. Chem.* **2008**, *80*, 4651−4658.

(13) Talaga, D. S.; Li, J. Single-Molecule Protein Unfolding in Solid State Nanopores. *J. Am. Chem. Soc.* **2009**, *131*, 9287−9297.

(14) Hall, A. R.; Keegstra, J. M.; Duch, M. C.; Hersam, M. C.; Dekker, C. Translocation of Single-Wall Carbon Nanotubes Through Solid-State Nanopores. *Nano Lett.* **2011**, *11*, 2446−2450.

(15) Lan, W.-J.; Holden, D. A.; Zhang, B.; White, H. S. Nanoparticle Transport in Conical-Shaped Nanopores. *Anal. Chem.* **2011**, *83*, 3840−3847.
(16) Kim, J.; Gonzalez-Martin, A. Nanopore Membrane-based Electrochemical Immunoassay. *J. Solid State Electrochem.* **2009**, *13*, 1037−1042.
(17) Gershow, M.; Golovchenko, J. A. Recapturing and Trapping Single Molecules with a Solid-State Nanopore. *Nat. Nanotechnol.* **2007**, *2*, 775−779.
(18) Rossi, A. M.; Wang, L.; Reipa, V.; Murphy, T. E. Porous silicon Biosensor for Detection of Viruses. *Biosens. Bioelectron.* **2007**, *23*, 741−745.
(19) Peh, A. E. K.; Li, S. F. Y. Dengue Virus Detection Using Impedance Measured across Nanoporous Alumina Membrane. *Biosens. Bioelectron.* **2013**, *42*, 391−396.
(20) Yanik, A. A.; Huang, M.; Kamohara, O.; Artar, A.; Geisbert, T. W.; Connor, J. H.; Altug, H. An Optofluidic Nanoplasmonic Biosensor for Direct Detection of Live Viruses from Biological Media. *Nano Lett.* **2010**, *10*, 4962−4969.
(21) Guo, P.; Hall, E. W.; Schirhagl, R.; Mukaibo, H.; Martin, C. R.; Zare, R. N. Microfluidic Capture and Release of Bacteria in a Conical Nanopore Array. *Lab Chip* **2012**, *12*, 558−561.
(22) Im, H.; Wittenberg, N. J.; Lesuffleur, A.; Lindquist, N. C.; Oh, S.-H. Membrane Protein Biosensing with Plasmonic Nanopore Arrays and Pore-Spanning Lipid Membranes. *Chem. Sci.* **2010**, *1*, 688−696.
(23) Dahlin, A. B.; Zäch, M.; Rindzevicius, T.; Käll, M.; Sutherland, D. S.; Höök, F. Localized Surface Plasmon Resonance Sensing of Lipid-Membrane-Mediated Biorecognition Events. *J. Am. Chem. Soc.* **2005**, *127*, 5043−5048.
(24) Eftekhari, F.; Escobedo, C.; Ferreira, J.; Duan, X.; Girotto, E. M.; Brolo, A. G.; Gordon, R.; Sinton, D. Nanoholes As Nanochannels: Flow-through Plasmonic Sensing. *Anal. Chem.* **2009**, *81*, 4308−4311.
(25) Escobedo, C.; Brolo, A. G.; Gordon, R.; Sinton, D. Flow-Through vs Flow-Over: Analysis of Transport and Binding in Nanohole Array Plasmonic Biosensors. *Anal. Chem.* **2010**, *82*, 10015−10020.
(26) Escobedo, C. On-chip Nanohole Array Based Sensing: a Review. *Lab Chip* **2013**, *13*, 2445−2463.
(27) Li, J.; Stein, D.; McMullan, C.; Branton, D.; Aziz, M. J.; Golovchenko, J. A. Ion-beam Sculpting at Nanometre Length Scales. *Nature* **2001**, *412*, 166−169.
(28) Nam, S.-W.; Rooks, M. J.; Kim, K.-B.; Rossnagel, S. M. Ionic Field Effect Transistors with Sub-10 nm Multiple Nanopores. *Nano Lett.* **2009**, *9*, 2044−2048.
(29) Storm, A. J.; Chen, J. H.; Ling, X. S.; Zandbergen, H. W.; Dekker, C. Fabrication of Solid-State Nanopores with Single-Nanometre Precision. *Nat. Mater.* **2003**, *2*, 537−540.
(30) Jonsson, M. P.; Dahlin, A. B.; Feuz, L.; Petronis, S.; Höök, F. Locally Functionalized Short-Range Ordered Nanoplasmonic Pores for Bioanalytical Sensing. *Anal. Chem.* **2010**, *82*, 2087−2094.
(31) Junesch, J.; Sannomiya, T.; Dahlin, A. B. Optical Properties of Nanohole Arrays in Metal−Dielectric Double Films Prepared by Mask-on-Metal Colloidal Lithography. *ACS Nano* **2012**, *6*, 10405−10415.
(32) Junesch, J.; Sannomiya, T. Reflection Phase and Amplitude Determination of Short-Range Ordered Plasmonic Nanohole Arrays. *J. Phys. Chem. Lett.* **2014**, *5*, 247−252.
(33) Hanarp, P.; Sutherland, D. S.; Gold, J.; Kasemo, B. Control of Nanoparticle Film Structure for Colloidal Lithography. *Colloids Surf., A* **2003**, *214*, 23−36.
(34) Danev, R.; Nagayama, K. Transmission Electron microscopy with Zernike Phase Plate. *Ultramicroscopy* **2001**, *88*, 243−252.
(35) Dahlin, A. B.; Sannomiya, T.; Zahn, R.; Sotiriou, G. A.; Vörös, J. Electrochemical Crystallization of Plasmonic Nanostructures. *Nano Lett.* **2011**, *11*, 1337−1343.
(36) Dahlin, A. B.; Tegenfeldt, J. O.; Höök, F. Improving the Instrumental Resolution of Sensors Based on Localized Surface Plasmon Resonance. *Anal. Chem.* **2006**, *78*, 4416−4423.
(37) Wittenberg, N. J.; Im, H.; Johnson, T. W.; Xu, X.; Warrington, A. E.; Rodriguez, M.; Oh, S.-H. Facile Assembly of Micro- and Nanoarrays for Sensing with Natural Cell Membranes. *ACS Nano* **2011**, *5*, 7555−7564.
(38) García de Abajo, F. J. Colloquium: Light Scattering by Particle and Hole Arrays. *Rev. Mod. Phys.* **2007**, *79*, 1267−1290.
(39) Sannomiya, T.; Scholder, O.; Jefimovs, K.; Hafner, C.; Dahlin, A. B. Investigation of Plasmon Resonances in Metal Films with Nanohole Arrays for Biosensing Applications. *Small* **2011**, *7*, 1653−1663.
(40) Ikenoya, Y.; Susa, M.; Shi, J.; Nakamura, Y.; Dahlin, A. B.; Sannomiya, T. Optical Resonances in Short-Range Ordered Nanoholes in Ultrathin Aluminum/Aluminum Nitride Multilayers. *J. Phys. Chem. C* **2013**, *117*, 6373−6382.
(41) Sannomiya, T.; Hafner, C. Multiple Multipole Program Modelling for Nano Plasmonic Sensors. *J. Comput. Theor. Nanosci.* **2010**, *7*, 1587−1595.
(42) Johnson, P. B.; Christy, R. W. Optical Constants of the Noble Metals. *Phys. Rev. B* **1972**, *6*, 4370−4379.
(43) Bochenkov, V. E.; Frederiksen, M.; Sutherland, D. S. Enhanced Refractive Index Sensitivity of Elevated Short-Range Ordered Nanohole Arrays in Optically Thin Plasmonic Au Films. *Opt. Express* **2013**, *21*, 14763−14770.
(44) Zhang, X.; Li, Z.; Ye, S.; Wu, S.; Zhang, J.; Cui, L.; Li, A.; Wang, T.; Li, S.; Yang, B. Elevated Ag Nanohole Arrays for High Performance Plasmonic Sensors Based on Extraordinary Optical Transmission. *J. Mater. Chem.* **2012**, *22*, 8903−8910.
(45) Najiminaini, M.; Vasefi, F.; Kaminska, B.; Carson, J. J. L. Nano-Hole Array Structure with Improved Surface Plasmon Energy Matching Characteristics. *Appl. Phys. Lett.* **2012**, *100*, 043105.
(46) Harumoto, T.; Sannomiya, T.; Matsukawa, Y.; Muraishi, S.; Shi, J.; Nakamura, Y.; Sawada, H.; Tanaka, T.; Tanishiro, Y.; Takayanagi, K. Controlled Polarity of Sputter-Deposited Aluminum Nitride on Metals Observed by Aberration Corrected Scanning Transmission Electron Microscopy. *J. Appl. Phys.* **2013**, *113*, 084306.
(47) Zan, H.-W.; Yen, K.-H.; Liu, P.-K.; Ku, K.-H.; Chen, C.-H.; Hwang, J. Low-Voltage Organic Thin Film Transistors with Hydrophobic Aluminum Nitride Film as Gate Insulator. *Org. Electron.* **2007**, *8*, 450−454.
(48) Kumar, S.; Wittenberg, N. J.; Oh, S.-H. Nanopore-Induced Spontaneous Concentration for Optofluidic Sensing and Particle Assembly. *Anal. Chem.* **2012**, *85*, 971−977.
(49) Vörös, J. The Density and Refractive Index of Adsorbing Protein Layers. *Biophys. J.* **2004**, *87*, 553−561.
(50) Sannomiya, T.; Balmer, T. E.; Heuberger, M.; Vörös, J. Simultaneous Refractive Index and Thickness Measurement with the Transmission Interferometric Adsorption Sensor. *J. Phys. D: Appl. Phys.* **2010**, *43*, 405302.
(51) Valsecchi, C.; Brolo, A. G. Periodic Metallic Nanostructures as Plasmonic Chemical Sensors. *Langmuir* **2013**, *29*, 5638−5649.
(52) Chen, P.; Mitsui, T.; Farmer, D. B.; Golovchenko, J.; Gordon, R. G.; Branton, D. Atomic Layer Deposition to Fine-Tune the Surface Properties and Diameters of Fabricated Nanopores. *Nano Lett.* **2004**, *4*, 1333−1337.
(53) Siwy, Z. S. Ion-Current Rectification in Nanopores and Nanotubes with Broken Symmetry. *Adv. Funct. Mater.* **2006**, *16*, 735−746.
(54) Kovarik, M. L.; Zhou, K.; Jacobson, S. C. Effect of Conical Nanopore Diameter on Ion Current Rectification. *J. Phys. Chem. B* **2009**, *113*, 15960−15966.
(55) Harding, I. H. Amphoteric Polystyrene Latex Colloids: Polymerization Pathway and the Control of Particle Size and Potential. *Colloid Polym. Sci.* **1985**, *263*, 58−66.
(56) Voss, B.; Haase, M. Intrinsic Focusing of the Particle Size Distribution in Colloids Containing Nanocrystals of Two Different Crystal Phases. *ACS Nano* **2013**, *7*, 11242−11254.
(57) Hawkeye, M. M.; Brett, M. J. Glancing Angle Deposition: Fabrication, Properties, and Applications of Micro- and Nanostructured Thin Films. *J. Vac. Sci. Technol., A* **2007**, *25*, 1317−1335.

(58) Wanunu, M.; Dadosh, T.; Ray, V.; Jin, J.; McReynolds, L.; Drndic, M. Rapid Electronic Detection of Probe-Specific MicroRNAs Using Thin Nanopore Sensors. *Nat. Nanotechnol.* **2010**, *5*, 807−814.
(59) Chen, Y.; Freunberger, S. A.; Peng, Z.; Fontaine, O.; Bruce, P. G. Charging a Li−O2 Battery Using a Redox Mediator. *Nat. Chem.* **2013**, *5*, 489−494.
(60) Peng, Z.; Freunberger, S. A.; Chen, Y.; Bruce, P. G. A Reversible and Higher-Rate Li-O2 Battery. *Science* **2012**, *337*, 563−566.
(61) Chen, L.; Gu, Q.; Zhou, X.; Lee, S.; Xia, Y.; Liu, Z. New-concept Batteries Based on Aqueous Li+/Na+ Mixed-ion Electrolytes. *Sci. Rep.* **2013**, *3*, 1−7.
(62) Bruce, P. G.; Freunberger, S. A.; Hardwick, L. J.; Tarascon, J.-M. Li-O2 and Li-S Batteries with High Energy Storage. *Nat. Mater.* **2012**, *11*, 19−29.
(63) Dahlin, A. B.; Wittenberg, N. J.; Höök, F.; Oh, S.-H. Promises and Challenges of Nanoplasmonic Devices for Refractometric Biosensing. *Nanophotonics* **2013**, *2*, 83−101.
(64) Lemay, S. G.; van den Broek, D. M.; Storm, A. J.; Krapf, D.; Smeets, R. M. M.; Heering, H. A.; Dekker, C. Lithographically Fabricated Nanopore-Based Electrodes for Electrochemistry. *Anal. Chem.* **2005**, *77*, 1911−1915.
(65) Zhang, Y.; Zhang, B.; White, H. S. Electrochemistry of Nanopore Electrodes in Low Ionic Strength Solutions. *J. Phys. Chem. B* **2006**, *110*, 1768−1774.
(66) Sexton, L. T.; Horne, L. P.; Martin, C. R. Developing Synthetic Conical Nanopores for Biosensing Applications. *Mol. BioSyst.* **2007**, *3*, 667−685.
(67) Vlassiouk, I.; Apel, P. Y.; Dmitriev, S. N.; Healy, K.; Siwy, Z. S. Versatile Ultrathin Nanoporous Silicon Nitride Membranes. *Proc. Natl. Acad. Sci. U. S. A.* **2009**, *106*, 21039−21044.
(68) Simon, A.; Girard-Egrot, A.; Sauter, F.; Pudda, C.; Picollet D'Hahan, N.; Blum, L.; Chatelain, F.; Fuchs, A. Formation and Stability of a Suspended Biomimetic Lipid Bilayer on Silicon Submicrometer-Sized Pores. *J. Colloid Interface Sci.* **2007**, *308*, 337−343.
(69) Korman, C. E.; Megens, M.; Ajo-Franklin, C. M.; Horsley, D. A. Nanopore-Spanning Lipid Bilayers on Silicon Nitride Membranes That Seal and Selectively Transport Ions. *Langmuir* **2013**, *29*, 4421−4425.
(70) Reimhult, E.; Kumar, K. Membrane Biosensor Platforms Using Nano- and Microporous Supports. *Trends Biotechnol.* **2008**, *26*, 82−89.